IOP Publishing and International Atomic Energy Agency Nuclear Fusion
Nucl. Fusion **52** (2012) 094001 (14pp) doi:10.1088/0029-5515/52/9/094001

Study of chirping toroidicity-induced Alfvén eigenmodes in the National Spherical Torus Experiment

M. Podestà[1], R.E. Bell[1], A. Bortolon[2], N.A. Crocker[3], D.S. Darrow[1], A. Diallo[1], E.D. Fredrickson[1], G.-Y. Fu[1], N.N. Gorelenkov[1], W.W. Heidbrink[2], G.J. Kramer[1], S. Kubota[3], B.P. LeBlanc[1], S.S. Medley[1] and H. Yuh[4]

[1] Princeton Plasma Physics Laboratory, Princeton NJ 08543, USA
[2] Department of Physics and Astronomy, University of California, Los Angeles, CA 90095, USA
[3] Department of Physics and Astronomy, University of California, Irvine, CA 92697, USA
[4] Nova Photonics, Princeton NJ 08543, USA

E-mail: mpodesta@pppl.gov

Received 30 December 2011, accepted for publication 12 March 2012
Published 3 September 2012
Online at stacks.iop.org/NF/52/094001

Abstract
Chirping toroidicity-induced Alfvén eigenmodes (TAEs) are destabilized during neutral beam injection on the National Spherical Torus Experiment (NSTX (Ono M. *et al* 2000 *Nucl. Fusion* **40** 557)) by super-Alfvénic ions with velocities up to five times larger than the Alfvén velocity. TAEs exhibit repeated bursts in amplitude and down-chirps in frequency. Larger bursts, so-called TAE *avalanches*, are eventually observed and correlate with a loss of fast ions up to 30% over ∼1 ms. Frequency, amplitude and radial structure of TAEs are characterized via magnetic pickup coils and a multi-channel reflectometer system. The modes have a broad radial structure, which appears to be unaffected by the large frequency and amplitude variations. However, the large mode amplitude does impact the modes' dynamics by favouring the coupling among different modes. In addition, the coupling involves kink-like modes and can therefore degrade the thermal plasma confinement. In spite of the non-linear regime characterizing the TAE dynamics, the measured properties are found to be in reasonable agreement with solutions from the ideal MHD code NOVA.

(Some figures may appear in colour only in the online journal)

1. Introduction

The enhanced fast ion transport caused by multiple toroidicity-induced Alfvén eigenmodes (TAEs [1]) is believed to be one of the main loss mechanisms for fast ions in ITER [2]. Enhanced losses reduce the fusion efficiency and may cause harm to in-vessel structures. Understanding this phenomenon in order to limit, or possibly avoid, its deleterious effects in future reactors is therefore paramount for fast ion research [3]. One key aspect for predicting TAE behaviour and associated losses is the type of wave–particles interaction in velocity space. Single TAEs have already been observed to interact strongly with the fast ion population, resulting in the splitting of the original mode into multiple branches [4], or in periodic variations of its frequency (*chirps*) [5, 6]. Of more concern is the overlap of multiple resonances in phase space [7], because broad regions of the fast ion distribution can provide enough free energy to sustain an explosive growth of the instabilities [8]. These rapid events are characterized by short time scales, $\lesssim$1 ms, for which no possibility of *external* control (e.g. through tailored injection of neutral beams or rf waves) presently exists. Therefore, they will be a particularly severe issue for future devices. In the following, these two cases are referred to as *single-mode* and *multi-mode* regimes.

Typical scenarios on the National Spherical Torus Experiment (NSTX) [9] are considerably different from those predicted for ITER and future reactors. Nonetheless, they provide a good test case to improve the present understanding of the basic physics of bursting TAEs. TAE bursts with duration ∼1 ms are commonly observed in NSTX neutral beam-heated plasmas and can cause up to 30% loss of the confined fast ion population in a single event [10, 11]. NSTX

plasmas can therefore be used to challenge present theories and numerical codes, with the overall goal of improving our predictive capabilities.

Comparisons between experiments and codes are usually done in terms of the modes' properties and dynamics for varying plasma conditions. A detailed study of TAE properties on NSTX, such as frequency, mode number and radial structure, and of their eventual modification during the bursting/chirping phase, is the main goal of this paper. In addition, previous results indicate that mode–mode coupling is at play during large TAE bursts [12], thus determining the possible transition from the single- to multi-mode regime. When coupling occurs, low-frequency ($\lesssim$30 kHz) modes with toroidal mode number $n = 1, 2$ are often observed and can lead to a further enhancement of fast ion and thermal transport. The nature of these low-frequency fluctuations is briefly discussed in this paper, showing the potential for TAEs to interact with other classes of MHD modes.

The paper is organized as follows. The experimental scenario used for TAE studies on NSTX is described in section 2. General properties of individual TAE modes are then discussed in section 3. A more global picture of the TAE dynamics is then presented in section 4, where evidence of the coupling among TAE modes, and between TAE and low-frequency MHD modes, is also discussed. In section 5, a numerical analysis of the measured TAE properties (i.e. mode number, frequency and radial structure) is performed through the ideal MHD code NOVA [13]. Qualitative observations on the drive and damping mechanisms at play for TAE in NSTX are then discussed in section 6. Section 7 summarizes the main finding of this work and concludes the paper.

2. Experimental scenario, diagnostics and analysis techniques

NSTX operates with a toroidal field $\sim$0.5 T, with typical density (3–10) $\times$ 10^{19} m^{-3}, temperature $T_e \approx T_i \lesssim 1.5$ keV and central plasma rotation $f_{rot} \lesssim 40$ kHz. Neutral beam (NB) injection is the main heating system. The maximum total power is $P_{NB} = 7$ MW from three sources with adjustable injection energy $E_{inj} = 60$–95 keV. The resulting fast ion population is super-Alfvénic with velocities $1 < v_{fast}/v_{Alfven} < 5$. Fast ions provide the drive for a variety of Alfvénic instabilities, including TAEs [14]. The latter have toroidal mode number up to $n = 8$ and frequency $60 < f < 250$ kHz in the laboratory frame. An example of the L-mode plasma scenario used for TAE studies is shown in figure 1. Deuterium plasmas with 1–2.5 MW of injected NB power are mainly used. The level of injected NB power, along with the low density of these L-mode plasmas ($n_e \sim (3\text{–}4) \times 10^{19}$ m^{-3}), leads to a high ratio between fast ion and thermal plasma pressures, β_{fi}/β_{th} (β is the ratio between kinetic and magnetic energies), as inferred from the TRANSP code[5] (figure 1(*d*)). The reversed-shear safety factor profile, $q(R)$, evolves in time. Its minimum, q_{min}, decreases from 4 to $\approx$1 during the discharge (figure 1(*c*)). The safety factor is reconstructed through the Grad–Shafranov equilibrium code LRDFIT [15], constrained by the motional Stark effect (MSE [16]) measurements of the magnetic pitch. For the experimental conditions investigated in this work, overall uncertainties in the $q(R)$ reconstruction are $\Delta q \simeq 0.1$, mostly caused by different choices of the constraints imposed in the solution of the Grad–Shafranov equilibrium.

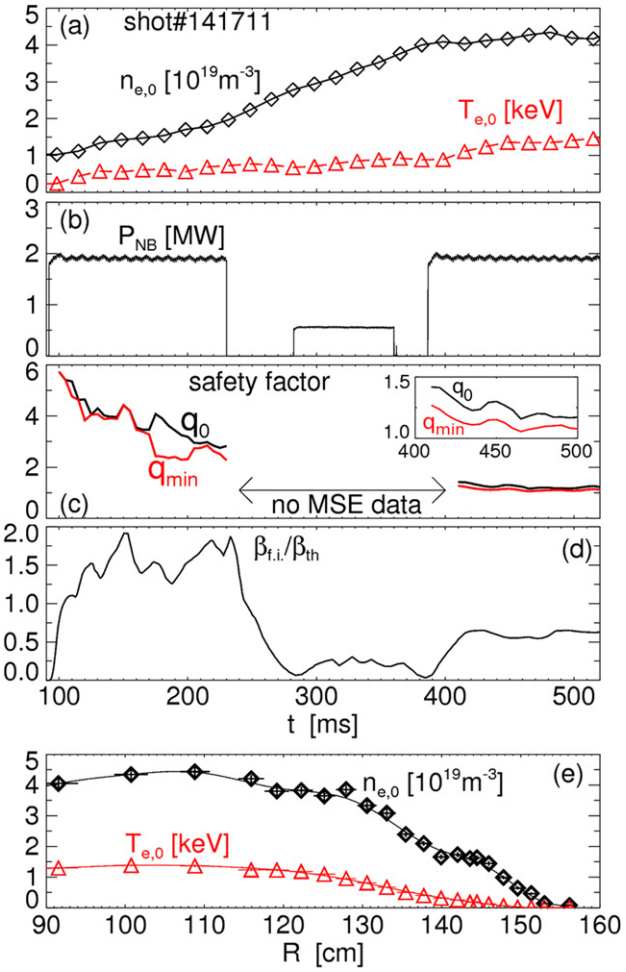

Figure 1. (*a*) Central electron density and temperature for NSTX discharge no 141711. (*b*) Injected NB power. (*c*) Central and minimum values of the safety factor, q_0 and q_{min}. No data are available for $t = 250$–410 ms. The inset shows an expanded view of the evolution of q_0 and q_{min} after 410 ms. (*d*) Ratio of fast ion to thermal β's, calculated through the TRANSP code. (*e*) Profiles of electron density and temperature at $t = 470$ ms. The magnetic axis is at $R \approx 105$ cm.

Time-resolved profiles of electron/ion density and temperature are obtained through Thomson scattering [17] and charge-exchange recombination spectroscopy [18] diagnostics that cover the full plasma minor radius. Time resolution is 16 ms and 10 ms, respectively.

Magnetic fluctuations are measured by an array of 11 toroidally distributed Mirnov coils, located at the vessel wall on the low-field side. Sampling frequency is 4 MHz. When a time resolution $\gtrsim$1 ms is sufficient, Mirnov coils data are analysed with standard techniques based on the fast Fourier transform (FFT). This provides time-dependent spectra of the modes' frequency and toroidal mode number, n, inferred from the phase variation as a function of the toroidal angle.

Higher-order Fourier analysis techniques, such as *bicoherence* analysis [19], are used to investigate mode–mode

[5] http://w3.pppl.gov/transp/

interactions. The bicoherence, $b(f_1, f_2|f_3)$, quantifies the degree of correlation between triplets of modes at frequency f_1, f_2 and f_3 via a phase-weighted average of the complex Fourier bispectrum. Frequencies of each triplet are such that $f_3 = f_1 \pm f_2$. Because of the normalization to the spectral amplitude, the analysis is independent of the actual mode amplitude and can reveal coupling among very weak modes, not directly observed in the Fourier spectrum. By summing $b(f_1, f_2|f_3)$ over all pairs (f_1, f_2) that contribute to a same f_3, the *total bispectrum* is obtained. This quantity is an estimate of how much spectral power at a given frequency is associated with bi-linear interactions between modes.

Because of its limitation in temporal resolution due to the lack of statistics for events of short duration, FFT analysis has limited use in the study of transient events lasting hundreds of microseconds or less. Instead, based on the naturally occurring frequency separation between modes (see section 3.1), an analysis based on band-pass filtering of the time series from Mirnov coils is used to resolve fast events. Signals are band-pass filtered around the frequency of each mode to obtain the corresponding fluctuations, $\dot{s}_n(t)$, and the B-field fluctuation signals, $s_n(t)$, through software integration of $\dot{s}_n(t)$. The evolution of frequency and amplitude, f_n and A_n, is then calculated from the peak-to-peak amplitude and peak separation of the resulting (sinusoidal) $s_n(t)$.

This analysis can be further developed to study mode–mode coupling over short time scales. In essence, the signal $s_n(t)$ is converted into its analytical (or complex) equivalent $\hat{h}_n(t) = s_n(t) + \mathrm{i}H\{s_n(t)\}$, where i is the imaginary unit and $H\{\cdot\}$ denotes Hilbert transform. Then, sub-samples of $\hat{h}_n(t)$ containing only a few fluctuation cycles for all potential frequencies (or n's) of interest are used to construct a *pseudo-spectrum* with amplitude $|\hat{h}_n|$ and phase $\tan^{-1}(\Im\{\hat{h}_n\}/\Re\{\hat{h}_n\})$ ($\Im\{\cdot\}$ and $\Re\{\cdot\}$ are the imaginary and real parts). The pseudo-spectrum is finally used to compute the bicoherence, with the advantage that short time series provide sufficient statistics to obtain reliable results over 100–200 μs intervals.

In addition to the information on fluctuations at the plasma edge from Mirnov coils, internal measurements of the radial structure of Alfvénic modes and of its temporal evolution are available from a multi-channel reflectometer system [20]. It measures path length variations of a probe microwave signal resulting from plasma density fluctuations. The system has 16 channels, tuned at different frequencies. Depending on the density profile, hence on the location of the cut-off radius for each specific frequency (channel), density fluctuations at up to 16 radial points can be measured. For the L-mode scenario investigated here, there are typically 9–11 radial points available. The analysis of reflectometer data is performed assuming small density fluctuations around an unperturbed density profile and linear propagation of the ordinary-mode polarized probe waves based on a one-dimensional model. Reflectometer's data are inverted using Gaussian basis functions centred around each measurement location to model density fluctuations. Each basis function is scaled until the simulated and measured path length variations match at all locations. Because density profile and its radial gradient are available every 16 ms, their possible variation on faster time scales is not accounted for in the analysis. This is the main source of uncertainties for the calculated density fluctuations, which can be as high as 20% of the relative fluctuations for events such as avalanches.

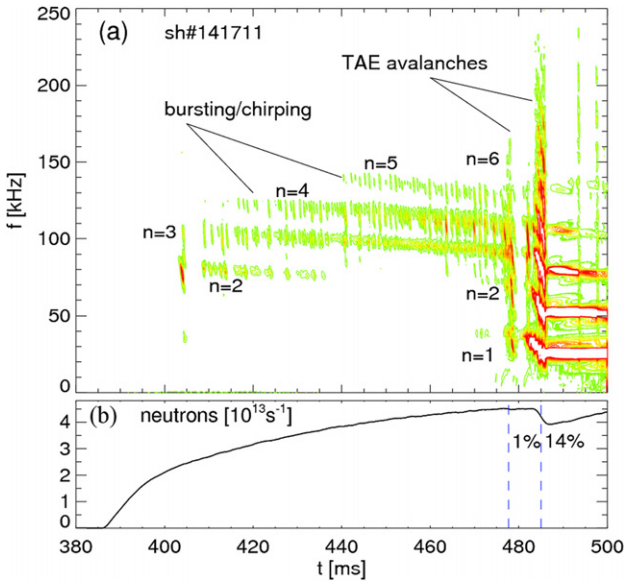

Figure 2. (*a*) Spectrum of magnetic field fluctuations from Mirnov coils showing TAEs with $f = 60$–150 kHz. (*b*) Neutron rate showing two drops associated with TAE avalanches. Because the main contribution to neutron rate is from beam-plasma reactions, relative drops in neutron rate are approximately equal to the fractional depletion of fast ions.

3. Characterization of single-mode TAE dynamics

3.1. Frequency and amplitude evolution

So far, most of the TAE studies on NSTX have been conducted in NB-heated, L-mode plasmas. These discharges are characterized by a high ratio $\beta_{\mathrm{fi}}/\beta_{\mathrm{th}}$ (figure 1(*d*)), which provides enough drive to destabilize TAEs. A spectrum of magnetic fluctuations, measured by Mirnov coils for the discharge in figure 1, is shown in figure 2(*a*). Bursts of TAEs correlate with frequency variations <10 kHz for $t < 480$ ms. Bursts repeat with a period of 0.5–2 ms, whose duration is rather independent of thermal plasma parameters or injected NB power. Eventually, larger bursts with frequency down-chirp >10 kHz lead to a so-called TAE *avalanche* [11]. Avalanches cause significant fast ion losses [10], as inferred from drops in the neutron rate, cf figure 2(*b*).

The spectrum of toroidal mode numbers, n, is shown in figure 3. The dominant modes for this discharge have $n = 3, 4$. Higher n's are observed at increasing frequencies, with very weak $n = 6, 7$ modes detected up to $f \sim 200$ kHz.

Taking the frequency variation as indicative of the severity of a burst, the relationship between measured frequency chirp and $\beta_{\mathrm{fi}}/\beta_{\mathrm{th}}$ is shown in figure 4 for a set of discharges with different density and injected NB power. Only cases without large, low-frequency MHD activity associated with kink-like modes, causing transient and non-reproducible drops in β_{fi} and β_{th}, are included. The fractional frequency chirp is calculated with respect to the mode frequency in the plasma frame. Large frequency chirps and amplitude excursions are mostly observed for larger values of $\beta_{\mathrm{fi}}/\beta_{\mathrm{th}}$. However, there is still a

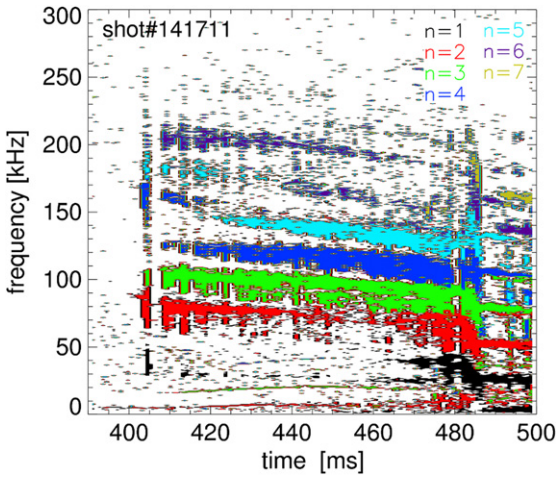

Figure 3. Toroidal mode number spectrum for the discharge shown in figure 2. Note the $n = 5$–7 modes at $f > 150$ kHz, which are not apparent in figure 2(a) because of their very weak amplitude.

considerable fraction of bursts with relatively mild amplitude and frequency excursions at high $\beta_{\rm fi}/\beta_{\rm th}$. This suggests that the fast ion drive, which is roughly proportional to $\beta_{\rm fi}$, is only one of the parameters regulating the TAE dynamics, as expected for a semi-chaotic regime in which multiple drive and damping terms compete [8, 21]. It should be noted that, because NB injection provides central fuelling and heating in addition to being the fast ion source, it is in practice difficult to separate unambiguously the effects of $\beta_{\rm fi}$ and of $\beta_{\rm th}$ in these discharges. This can be appreciated from figure 4(d), showing a roughly linear relationship between $\beta_{\rm fi}$ and $\beta_{\rm th}$.

It should also be noted that, in addition to TAEs, modes with $n = 1$ and $f \sim 25$ kHz (that is, well below the TAE gap) are often detected during strong TAE bursts. These fluctuations have a duration comparable to, or larger than, that of the avalanches, indicating that they may also play a role in the fast ion loss process [12]. More details on the nature and role of these low-frequency fluctuations are given in section 4.

Further information on the properties of chirping TAEs can be gathered from a detailed analysis of the amplitude and frequency behaviour during the bursts for single modes. An example is illustrated in figure 5(a) for a $n = 3$ mode. A first conclusion is that frequency and amplitude evolutions are indeed correlated, with the peak amplitude of each burst measured at about half the frequency sweep duration. Then, amplitude decays toward the noise level while the frequency continues to decrease. Eventually, a new burst begins with a rapid amplitude growth. At this point, the frequency jumps up by several kHz's and the cycle repeats. Different models have been proposed to explain the repeated bursts and chirps of the modes. Arguably, the most successful in reproducing the features observed experimentally are those based on generalizations of the *bump-on-tail* problem (cf [8, 21, 22] and references therein), which consider the formation of hole–clump pairs in the fast ion velocity space. The response of the modes to this perturbation results in a characteristic evolution of the frequency, namely $f \propto \pm\sqrt{t}$ for both up- and down-chirping modes. Other models, originating from the so-called *tip model* [23], extend the hole–clump model to the case of modes that interact strongly with the TAE continuum during their frequency down-chirp [24]. In this case, the mode can undergo an asymptotic explosive growth with a time dependence $A(t) \propto (t_\infty - t)^{-1}$.

A comparison of these two classes of models with the experiments shows a qualitative agreement, see the example in figures 5(b)–(c). For instance, the mode's growth is compatible with a t^{-1} dependence, at least in the time window following the initial, slow amplitude increase and before saturation inhibits a further growth (consistently with the hypotheses in [24]). However, other time dependencies, such as a simple exponential, provide an equally good (if not better) fit to the data. Similarly, the $\sqrt{t}$ dependence resulting from the hole–clump models is consistent with the observed frequency evolution, but other functional forms are, in fact, equally close to the data. A second conclusion on the amplitude and frequency evolution is therefore that the models mentioned above are indeed compatible with the experiments, but they may not be uniquely identifiable, in the sense that other time dependencies could actually provide an equally good description of the data. For instance, the inclusion of additional physics can modify the temporal behaviour of TAEs resulting from the models. Experimentally, very limited or no information is presently available to investigate the fast ion profile variations on short ($\lesssim$1 ms) time scales and with sufficiently good spatial resolution. Different methods can, however, be utilized to study mode–mode coupling and the resulting multi-mode dynamics, see section 4.

3.2. Mode structure

A third important property of TAEs is their radial structure. For example, details on the mode structure can be used to distinguish between different classes of modes, such as reversed-shear Alfvén eigenmodes (RSAEs) and TAEs [25], and their transition from ideal MHD modes into energetic particle modes (EPMs). In addition, the radial extent of the modes partly determines the potential of the modes to cause fast ion losses from the confinement region, in contrast to redistribution *within* the main plasma in either real or velocity space.

An example of density fluctuations, $\delta n/n$, associated with a $n = 3$ mode at $f \approx 89$ kHz (cf figure 2(a)) is shown in figure 6. It demonstrates the potential of the reflectometer system for $\delta n/n$ results with high temporal resolution, as required for transient events such as TAE bursts and avalanches. The general features observed in figure 6 are common to low-n modes observed on NSTX. The modes have a broad radial structure, extending over a good fraction of the minor radius. The peak $\delta n/n$ is measured outside mid-radius, $R \gtrsim 120$ cm (the magnetic axis being at $R \approx 100$ cm). Noticeably, a non-vanishing $\delta n/n$ is found even for the outermost channels, which are just a few centimetres inside the last closed flux surface, indicating a finite mode amplitude in the proximity of the plasma boundary. The observed TAEs are therefore global modes, which are capable of interacting with the fast ion population over most of the plasma volume.

As a further step, the possible distortion of the mode structure during an avalanche is investigated (figure 7). Data refer to the times corresponding to the maximum mode activity of the three bursts that actually form the avalanche, as seen from the high time resolution spectrogram in figure 7(a). The

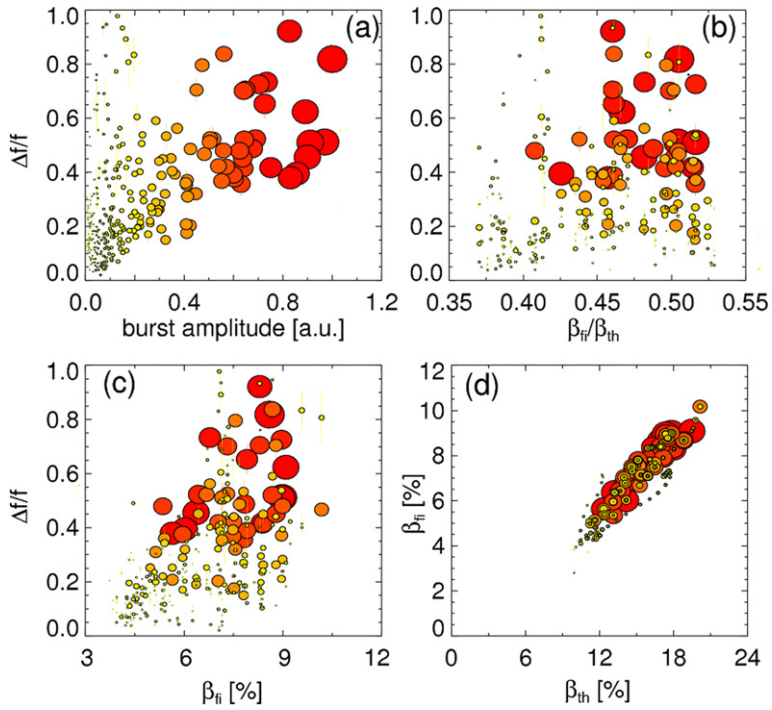

Figure 4. Parameter space for bursting/chirping TAEs in L-mode. Shown is the relative frequency variation, normalized to the mode frequency in the plasma frame, with respect to (*a*) the amplitude increase during the frequency chirp, (*b*) the ratio of central fast ion to plasma β and (*c*) the central fast ion β. (An example of time traces used to calculate frequency variation and burst amplitude is given in figure 5(*a*)). The parameter space as a function of $\beta_{\rm fi}$ and $\beta_{\rm th}$ is shown in panel (*d*), which reveals the coupling between those two parameters. In all panels the size of the symbols is proportional to the burst amplitude. Amplitudes typically measured at the plasma edge are $\delta B/B \sim 10^{-4}$, corresponding to ∼0.1 in the normalized units of burst amplitude in panel (*a*).

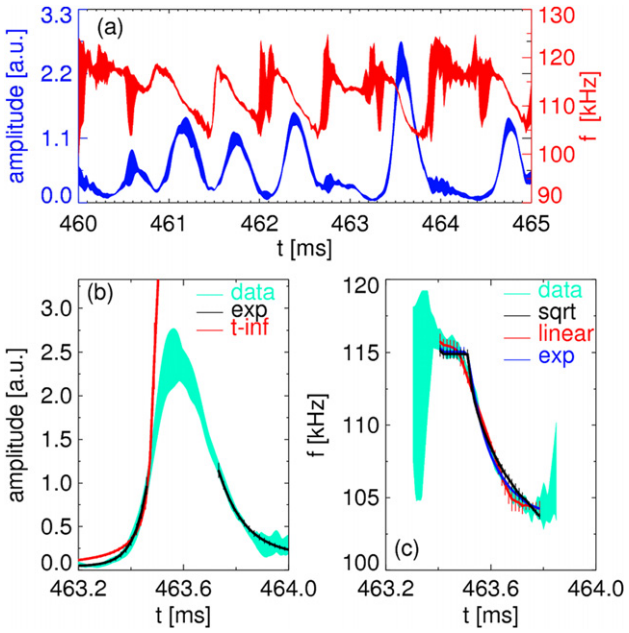

Figure 5. (*a*) Amplitude and frequency evolution around $t \approx 463$ ms for the $n = 3$ mode in figure 2. (*b*) Amplitude evolution during the bursts at 463.6 ms. Shaded area represents the experimental data from 11 Mirnov coils. Curves show a fit of the initial growth phase with an exponential (exp, also including a fit of the decaying mode amplitude) and a function $\sim 1/(t_\infty - t)$, representative of the explosive mode's growth (*t*-inf). (*c*) Frequency evolution from the experiment (shaded area), $f(t)$, and fit with three test models: $f \propto -\sqrt{t}$ (sqrt), $f \propto -t$ (linear) or $f \propto {\rm e}^{-t}$ (exp).

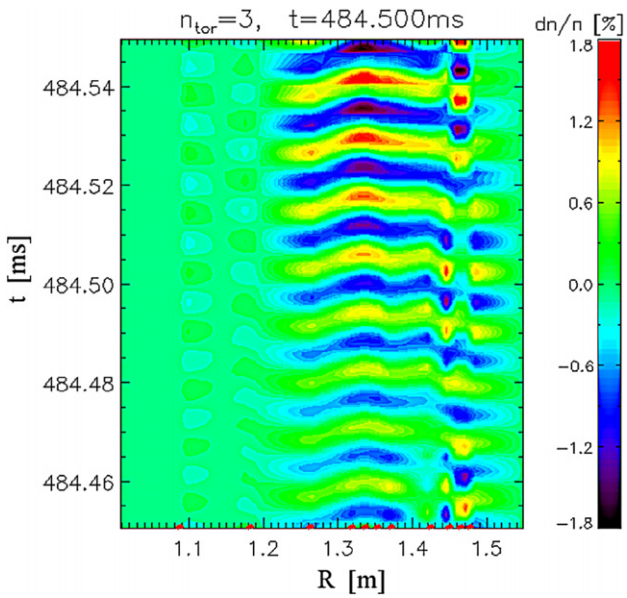

Figure 6. Density fluctuation, reconstructed from a multi-channel reflectometer system, for a $n = 3$ mode. The discharge is the same as in figure 2. Dots on the *x*-axis indicate the actual measurement locations. The magnetic axis and last closed flux surface are at $R = 102$ cm and $R = 152$ cm, respectively.

mode structure evolution during the avalanche is illustrated in figures 7(*b*)–(*e*) for modes with $n = 2 \ldots 5$. The reflectometer data show that, in spite of the large amplitude and frequency variations occurring during the avalanche, the mode

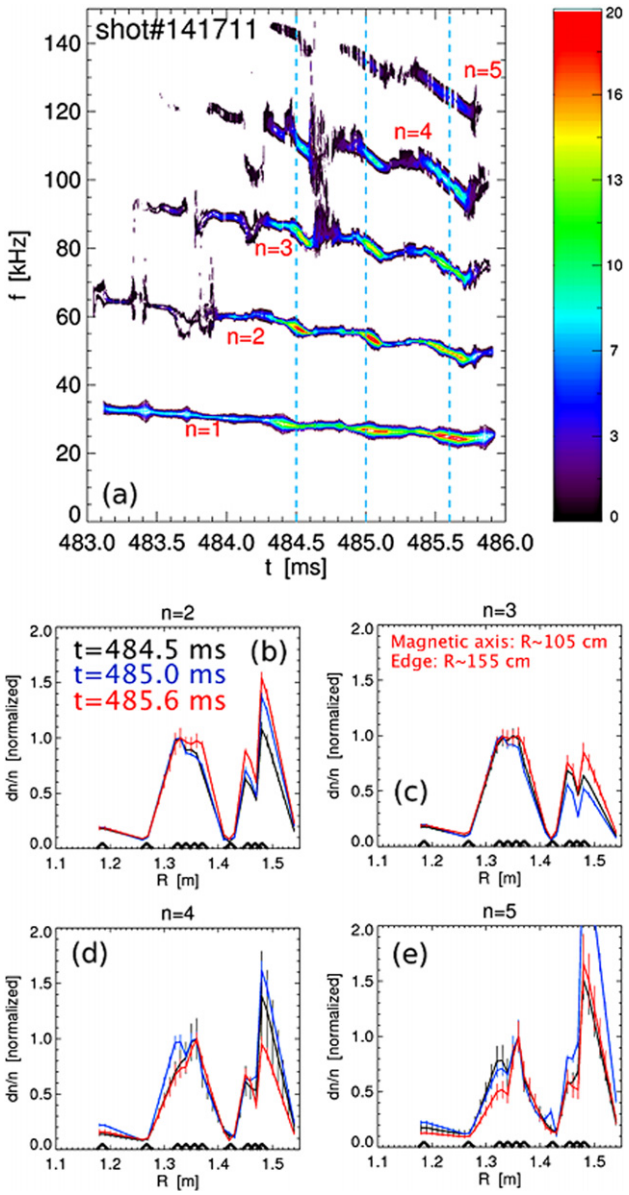

Figure 7. (*a*) Frequency and amplitude evolution during a TAE avalanche for discharge no 141711. (*b*)–(*e*) Reconstructed $\delta n/n$ at three stages of the burst, indicated by vertical dashed lines in panel (*a*), for $n = 2, \ldots, 5$. Note that amplitudes are rescaled so that $\max\{\delta n/n\} = 1$ for $130 \leqslant R \leqslant 140$ cm for a better comparison of the radial structure at different times.

structure does not vary significantly within the experimental uncertainties. Consistently with the model discussed in [26], the broad radial structure of the modes relative to the scale-lengths of the fast ion density profile is believed to inhibit here a macroscopic radial propagation of the mode.

4. Multi-mode TAE dynamics and interaction with low-frequency MHD modes

The TAE properties illustrated in the previous section refer to single, individual chirping modes. In this section, the interaction between modes and the overall multi-mode dynamics are considered. For example, a common feature of TAEs in NSTX L-mode plasmas, which is apparent in figure 3 for $n = 2, \ldots, 5$, is a roughly constant frequency separation between modes with consecutive n's [27]. This suggests that the modes share a common frequency in the plasma frame, $f_0^{\rm TAE}$, such that $f_{{\rm lab},n}^{\rm TAE} = f_0^{\rm TAE} + n\, f_{\rm Doppler}^{\rm TAE}$ [28]. Here $f_{{\rm lab},n}^{\rm TAE}$ is the frequency for the toroidal mode number n in the laboratory frame and $f_{\rm Doppler}^{\rm TAE}$ the Doppler shift caused by plasma rotation. Knowing $f_{\rm Doppler}^{\rm TAE}$ and the plasma rotation profile $f_{\rm rot}(R, t)$, measured through charge-exchange recombination spectroscopy (CHERS) of carbon rotation [18], the radius $R^{\rm TAE}$ such that $f_{\rm Doppler}^{\rm TAE} = f_{\rm rot}(R^{\rm TAE})$ can be calculated. In the following, $R^{\rm TAE}$ is referred to as the *characteristic radius* of the cluster of TAEs. For modes whose radial extension is much smaller than the minor radius, $R^{\rm TAE}$ represents the actual radial position of the cluster of modes and is expected to coincide with the radius of maximum mode amplitude [28]. However, this intuitive interpretation of $R^{\rm TAE}$ becomes less clear for more global modes which extend over a considerable fraction of the minor radius, such as the TAEs commonly observed on NSTX. In this case, $R^{\rm TAE}$ appears to be more related to the location of strongest drive of the modes, rather than to the exact radius of peak amplitude of each TAE (cf figures 6 and 9 in [27]). In general, one can interpret $R^{\rm TAE}$ as the characteristic radius where the local parameters (e.g. of the thermal plasma, fast ion population and/or of other instabilities) have the strongest influence on the evolution of the cluster of TAEs. The importance of $R^{\rm TAE}$ to understand the coupled dynamics of multiple TAEs is further discussed in section 6.

The accumulation of modes around the same radial location is one of the conditions potentially leading to coupling between modes. The total bispectrum for the shot in figure 2 is shown in figure 8, with details of the bicoherence calculated before and during a TAE avalanche (figures 8(*a*) and (*b*)). The bicoherence is small for small amplitude oscillations, indicating a weak or null coupling between modes which, nevertheless, still exhibit a bursting/chirping character. Conversely, values $\gtrsim$40% are obtained during the burst for frequencies corresponding to the TAEs and to other modes at $f < 60$ kHz and $f > 160$ kHz (figure 8(*b*)), indicating strong coupling at this time. The increase in the overall mode–mode coupling with time is observed in the total bispectrum (figure 8(*c*)), which shows enhanced values at all frequencies after $t \approx 460$ ms that culminate in the TAE avalanche.

A detail of the bicoherence evolution during short events is shown in figure 9. The analysis shows a finite bicoherence during some of the bursts and vanishing values for other times, in spite of the presence of multiple modes. This suggests that the mode–mode coupling strength varies on sub-millisecond time scales, thus confirming previous observations from NSTX [12]. Another result that was anticipated in [12] is the clear evidence of the coupling between TAE modes and low-frequency $n = 1, 2$ fluctuations. From the comparison with NOVA results, these modes are identified as kink-like modes (see the next section and [29] for a more exhaustive analysis).

For an efficient coupling, three-wave matching conditions, including phase coherence among the three waves, must be maintained for a sufficiently long time, of the order of tens of wave cycles of the primary (pump) modes, as observed in the experiments during the larger bursts. The

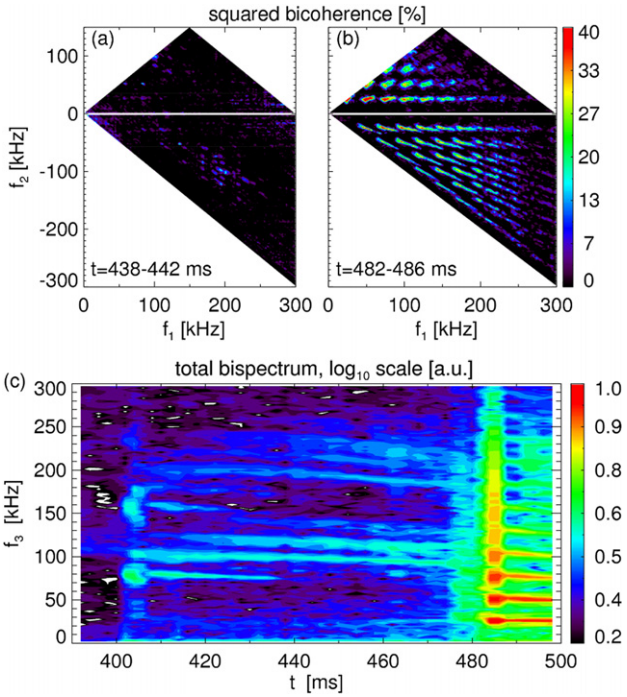

Figure 8. (*a*)–(*b*) Squared bicoherence at $t \approx 440$ ms (well before the TAE avalanche) and $t \approx 484$ ms (during the TAE avalanche) for the discharge in figure 2. The statistical noise level is $\lesssim 5\%$. Coupling among TAEs and between TAEs and low-frequency modes becomes evident for this latter case. (*c*) Total bispectrum, normalized to the range [0, 1]. (Analysis performed with 1024 FFT points, 4 ms time window, 50% overlap).

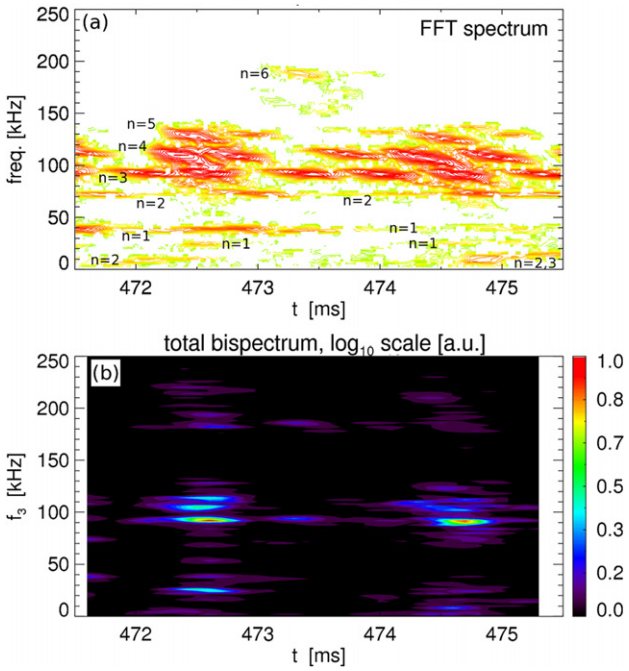

Figure 9. (*a*) FFT spectrogram. (*b*) Normalized total bispectrum around 473 ms (just before the TAE avalanche) obtained from the pseudo-spectrum of analytical signals (explanation in the text). Note the finite values during some of the bursts and the vanishing values at other times, in spite of the presence of multiple modes, indicating a non-constant level of mode–mode coupling on a sub-millisecond time scale.

particular relationship between frequencies (and, therefore, their clustering around a characteristic radius) of TAEs with subsequent n's, along with the presence of a seed $n = 1$ mode and a sufficiently strong drive, are thought to be other important ingredients for the development of bursting/chirping TAEs into avalanches. This hypothesis, supported by the results shown in figure 8, is tested in figures 10 and 11 for discharges where no TAE avalanches are observed in spite of the large number of chirping modes. In the first discharge (figure 10), strong low-frequency MHD activity is present but differs from what was discussed before. The dominant low-frequency mode has $n = 2$. Based on the flattening of thermal plasma profile around the $q = 2$ rational surface, it is tentatively identified as a large $m/n = 3/2$ island rotating at $\sim$20 kHz. Bicoherence and total bispectrum indicate that TAEs are interacting with these low-frequency modes, but no significant coupling among TAEs is measured, in contrast with the results shown in figure 8. This suggests that the criteria for an efficient mode–mode coupling, eventually leading to an avalanche, are not satisfied in this case. For instance, TAE modes may be localized around different radii and have mode structures that overlap only in part. The second discharge (figure 11) presents all the signatures that concur to originate an avalanche. Although relatively large frequency sweeps are observed, however, no large amplitude bursts and sudden drops in the neutron rate are measured. In this case, the missing ingredient is believed to be a strong enough drive of the modes, which keeps the TAEs close to marginal stability (cf section 6 and figure 17).

As a concluding remark for this section, we note that a recent theory on coupling between Alfvénic modes due

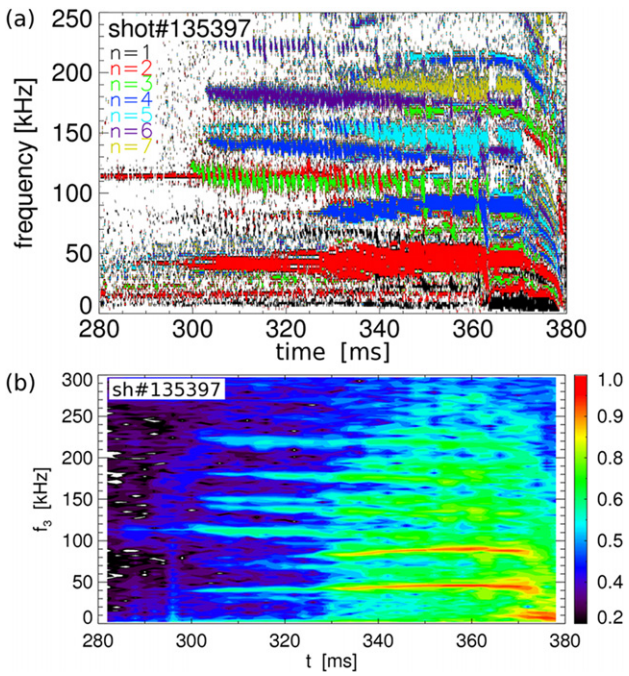

Figure 10. (*a*) Toroidal mode number spectrum for discharge no 135397. Note the large number of TAE modes with different n. In this case, the relationship $f^{\rm TAE}_{{\rm lab},n} = f^{\rm TAE}_0 + n\, f^{\rm TAE}_{\rm Doppler}$ is not satisfied. Low-frequency MHD with dominant $n = 2, 4$ at $f \approx 40$ kHz and $f \approx 80$ kHz is associated with a $m/n = 3/2$ island. (*b*) Total bispectrum. Colour code and amplitude scaling factor are the same as in figure 8(*c*).

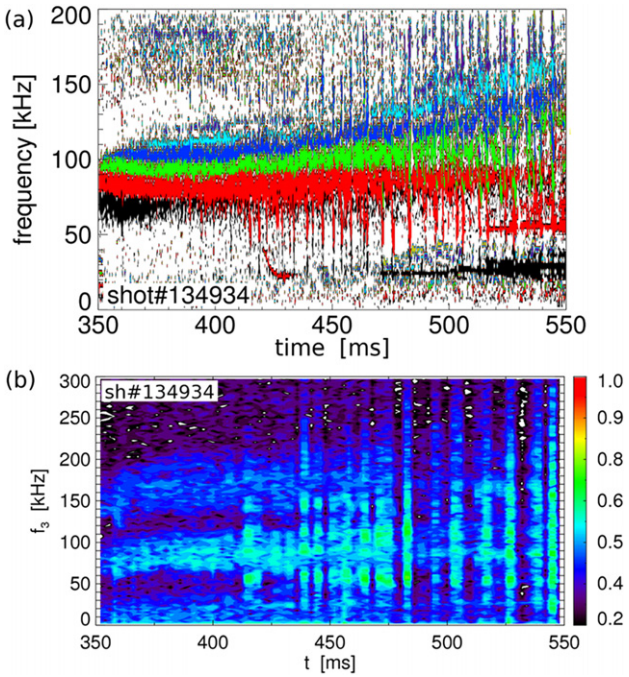

Figure 11. Same as in figure 10 for discharge no 134934. Here, $f^{\mathrm{TAE}}_{\mathrm{lab},n} = f^{\mathrm{TAE}}_{0} + n\, f^{\mathrm{TAE}}_{\mathrm{Doppler}}$ is verified and $n = 1$ activity is detected, but the fast ion drive is reduced with respect to figure 8.

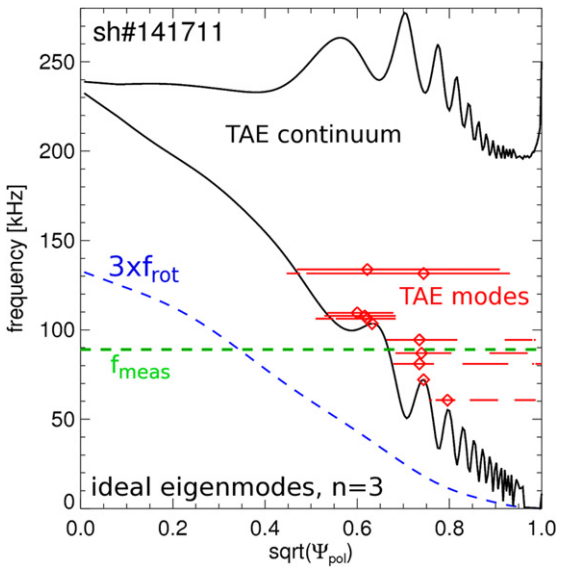

Figure 12. NOVA calculation of the TAE continuum and TAE/RSAE eigenmodes for $n = 3$ at $t = 470$ ms. The abscissa is the normalized minor radius, $\sqrt{\Psi_{\mathrm{pol}}} \sim r/a$ (Ψ_{pol} is the poloidal magnetic field flux). The measured frequency of the $n = 3$ mode, f_{meas}, is shown as a dashed line at $f = 89$ kHz. The Doppler shift frequency correction caused by plasma rotation, equal to $3 \times f_{\mathrm{rot}}(R)$ for $n = 3$, is also shown.

to perturbations of the axial symmetry [30] is qualitatively consistent with the coupling processes described above. A more quantitative study is left as future work.

5. Comparison with linear analysis from NOVA

In this section, the agreement between the measured mode properties and linear MHD theory is explored via the NOVA code ([13] and references therein). First, mode frequency and radial structure for the observed toroidal mode numbers are examined. Then, the analysis is extended in section 6 to a qualitative study of the damping terms from linear theory and fast ion drive from experimental observations.

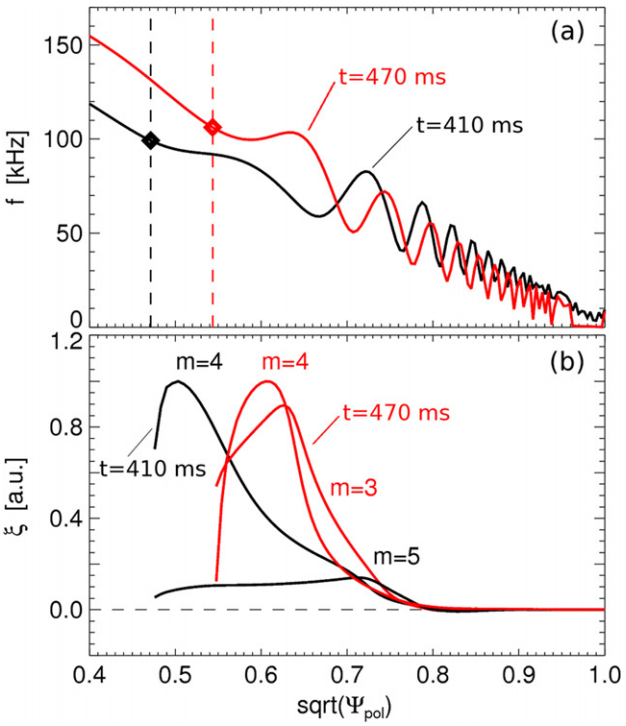

Figure 13. NOVA calculation of (*a*) TAE continuum and (*b*) radial displacement, ξ, for the two dominant poloidal harmonics (characterized by their poloidal mode number, m) for a $n = 3$ mode at two different times. The calculated mode shows a RSAE character early in the discharge and a transition into a TAE as β_{fi} increases. Only the harmonic structure inside the TAE gap is shown. Vertical dashed lines in (*a*) indicate where the modes intersect the lower TAE continuum.

NOVA analysis is based on the experimental plasma profiles at a fixed time. Toroidal rotation is included as a Doppler shift contribution to the mode frequency. The calculated $n = 3$ TAE continuum for the discharge in figure 2 at $t = 470$ ms, i.e. just before the TAE avalanche occurs, is illustrated in figure 12. The eigenmodes found by NOVA are shown in the same figure for the frequency range 60–140 kHz, with the measured mode frequency for $n = 3$ being 90–100 kHz. The code finds a large number of modes, which can be classified as TAE/RSAE and *continuum* modes. Unlike TAE/RSAE modes, the latter modes are characterized by a strong interaction with the TAE continuum (resulting in a discontinuity in the mode structure in ideal MHD theory). In practice, they are expected to be stable in the experiments and are not further discussed in the following.

From the many (ideal) eigenmodes found by NOVA, the best fit to the experimental mode is selected based on the agreement with the measured mode number, frequency and $\delta n/n$ profile, as detailed in [11]. The procedure can be repeated at different times to model the evolution of a single mode as the plasma parameters evolve. An example is shown in figure 13, which compares the dominant poloidal harmonics of a $n = 3$ mode at two different times. In both cases the mode intersects

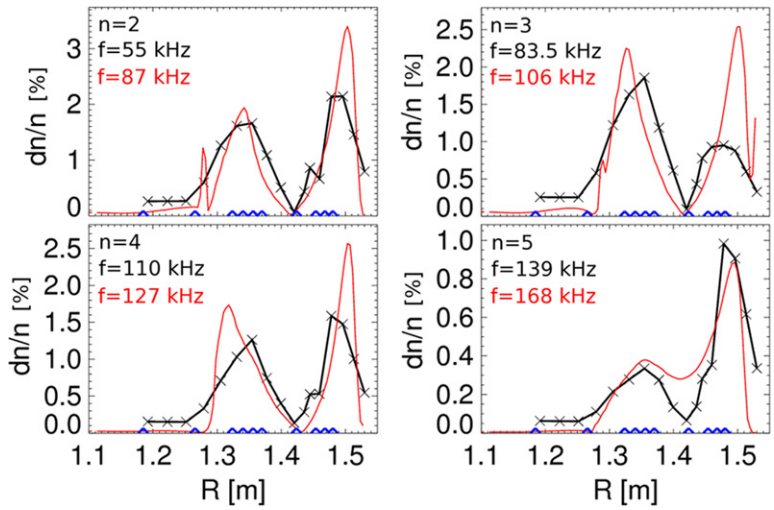

Figure 14. Comparison between $\delta n/n$ measured (solid, cross) and calculated by NOVA (solid, red) for $n = 2 \ldots 5$. Experimental profiles at $t = 470$ ms are used for the NOVA calculation, whereas data refer to $t \approx 484$ ms, during the avalanche phase.

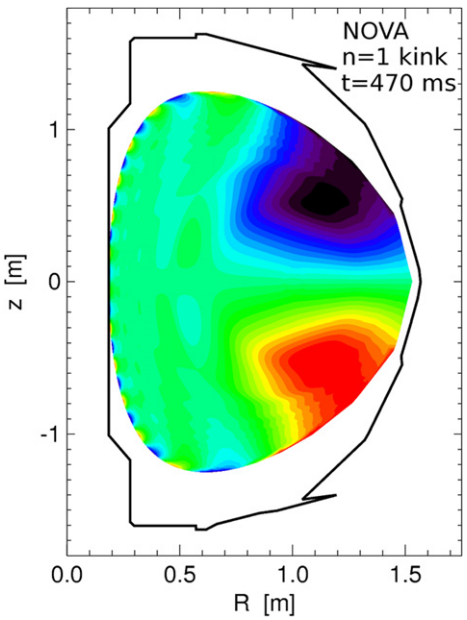

Figure 15. NSTX cross-section with two-dimensional profile of density fluctuations as calculated by the linear MHD code NOVA for an unstable $n = 1$ kink mode with $f \approx 0$ in the plasma frame.

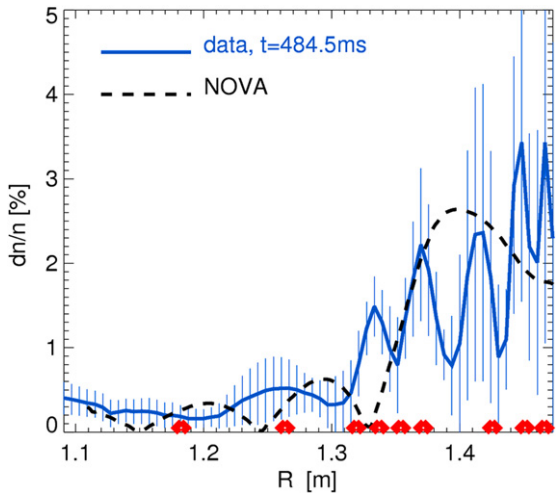

Figure 16. Measured (solid line) and simulated (dashed line) density perturbation associated with a $n = 1$ mode at mid-plane. Simulations are performed with the NOVA code, cf figure 15. Dots on the x-axis indicate the actual measurement locations.

the continuum around mid-radius. The total mode structure is similar for the two times. By looking at the poloidal harmonic composition, one can see that the mode has a dominant RSAE character early in time, with a single dominant m, then evolves into a TAE, characterized by two harmonics with comparable amplitude. This evolution is quite common on NSTX, and is attributed to a suppression of the RSAE modes as the plasma β_{th} increases [25], thus favouring the appearance of TAE modes instead.

By knowing the experimental profiles and the mode structure from NOVA, the corresponding (normalized) density perturbations can be calculated and rescaled to the $\delta n/n$ measured by the reflectometer. The comparison between measured and modelled density fluctuations is reported in figure 14. Considering that the ideal model does not include the self-consistent kinetic effects from fast ions, the modelled $\delta n/n$ is in fair agreement with the measurements for modes with $n = 2, \ldots, 5$. In turn, poor agreement is found for the low-frequency $n = 1$ mode.

Based on the upgraded reflectometer system, the density fluctuation resulting from the $n = 1$ mode has been measured and compared with NOVA calculations for ideal kink modes. No solutions are found for the standard, fixed-boundary version of the code, which assumes vanishing mode amplitude at the plasma edge (separatrix). When the fixed-boundary constraint is relaxed, a kink mode is found, see figure 15. The mode causes large edge perturbations, which is qualitatively consistent with the experimental observations (figure 16). This supports the interpretation of the $n = 1$ fluctuation as a kink-like mode. Additional analysis discussed in [29] strengthen this interpretation. Further studies will include fast ion effects in the simulation to investigate whether the mode is an ideal kink or a energetic-particle driven fishbone mode.

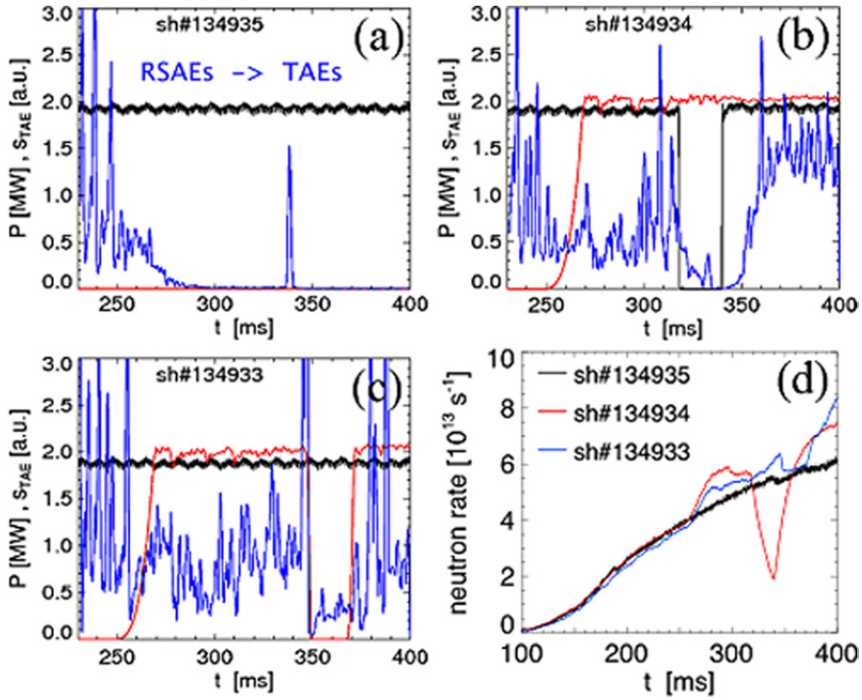

Figure 17. Effect of different heating schemes on TAE dynamics. (*a*) NB only. (*b*) and (*c*) NB+rf with a notch in NB and rf power, respectively. Modes before $t \approx 250$ ms are reverse-shear Alfvén eigenmodes, which then transition into TAEs. (*d*) Neutron rate showing increased reactivity once rf is turned on.

6. Role of drive and damping

As discussed in the previous sections, the observed TAEs are in a saturated, possibly non-linear regime characterized by a large variety of mutual interactions among TAEs themselves and between TAEs and other types of modes. The main factor determining this scenario is the drive provided by fast ions from NB injection. A first example of dependence of mode dynamics on fast ion population is given in figure 17, where the fast ion profile is perturbed using different heating schemes, including NB only and NB + rf injection. The reference discharge has NB injection only (figure 17(*a*)). The companion discharges have both NB+rf injection, with a notch of 20 ms in the NB power (figure 17(*b*)) and in the rf power (figure 17(*c*)). As the figures show, NB injection alone is insufficient to drive TAEs unstable in this case. When rf is added, the fast ion population slightly increases, as observed from the raise in neutron rate (figure 17(*d*)), and the modes are destabilized. It is plausible to assume that TAEs remain close to marginal stability, as suggested by the fact that their amplitude drops to noise level as soon as either NB or rf injection is interrupted. A noticeable result is the prompt onset of the bursting/chirping regime, indicating how easily the modes enter in this phase, at least for NSTX plasmas, once they are driven unstable.

A link between mode dynamics and fast ion population can be established experimentally by measuring the fast ion profile and its temporal evolution, e.g. through fast ion D-alpha (FIDA) spectroscopy [31, 32]. The correlation between TAEs and their drive is discussed in figure 18(*a*), where the calculated R^{TAE} (cf section 3.1) is compared with the position of steepest fast ion gradient. The two locations are similar, indicating that the shape of the fast ion profile plays a primary role in determining the localization (and, possibly, the dynamics) of TAEs. These observations may be used to design tools to affect the fast ion, hence the TAE, dynamics, for instance by varying the NB deposition profile and/or by means of localized rf deposition. (The maximum toroidal rotation shear is also located at the same radius, although it has been shown that rotation shear does not affect the macroscopic mode dynamics, cf [27]). The dependence upon the location of steepest fast ion gradient is believed to be responsible for the clustering of multiple modes around the same radius. The strong NB source term can efficiently sustain a steep, localized fast ion gradient, thus paving the way for mutual interactions between strongly unstable modes [12].

A departure of the characteristic radius of the TAE cluster, R^{TAE}, from the steepest fast ion gradient region is observed during the avalanche phase around $t = 480$ ms, (figures 18(*a*) and 19). At this time, the calculated R^{TAE} shifts towards the magnetic axis and $f_0^{\mathrm{TAE}}(R^{\mathrm{TAE}}) \to 0$, with $f_{\mathrm{lab},n}^{\mathrm{TAE}} \approx n\, f_{\mathrm{Doppler}}^{\mathrm{TAE}}(R^{\mathrm{TAE}})$, see figure 19(*a*). The comparison of measured $f_{\mathrm{lab},n}^{\mathrm{TAE}}$ against the values inferred from the fit $f_0^{\mathrm{TAE}} + n\, f_{\mathrm{Doppler}}^{\mathrm{TAE}}$ shows that the simple, linear relationship for the mode frequencies can reproduce satisfactorily the measured $f_{\mathrm{lab},n}^{\mathrm{TAE}}$. Note that $f_0^{\mathrm{TAE}} \to 0$ is satisfied at $R = R^{\mathrm{TAE}}$ because of a change in R^{TAE}, which does not necessarily imply a large change of the actual TAE frequency or radial mode structure, consistently with the results shown in figure 7.

Because toroidal rotation can undergo rapid, transient changes during large mode chirps due to the non-ambipolar loss of fast ions [33, 34], the sensitivity of these results to the fast evolution of f_{rot} is studied. By comparing figures 19(*a*) and (*b*), frequency changes do not appear to be directly synchronized with the neutron rate drop, hence the sudden reduction in rotation [33], as it would be expected if the

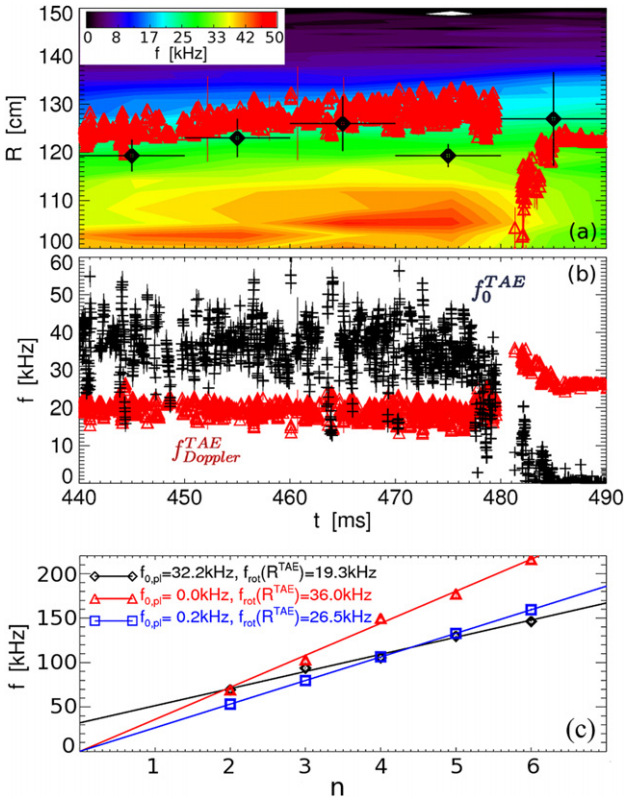

Figure 18. (*a*) Toroidal rotation for discharge no. 141711. Black diamonds indicate the position of steepest fast ion gradient. Red triangles show the evolution of $R^{\rm TAE}$. Note the large shift of $R^{\rm TAE}$ at $t \approx 480$ ms, when a TAE avalanche occurs. (*b*) Calculated $f_0^{\rm TAE}$ and $f^{\rm TAE}_{\rm Doppler}$ at $R = R^{\rm TAE}$ as a function of time. (*c*) Examples of fits of the measured $f^{\rm TAE}_{{\rm lab},n}$ versus toroidal mode number, n, at three different times. Note that the inferred $f_0^{\rm TAE} = f_0^{\rm TAE}(R^{\rm TAE})$, given by the intersection of the linear fit with the y-axis, vanishes after the avalanche.

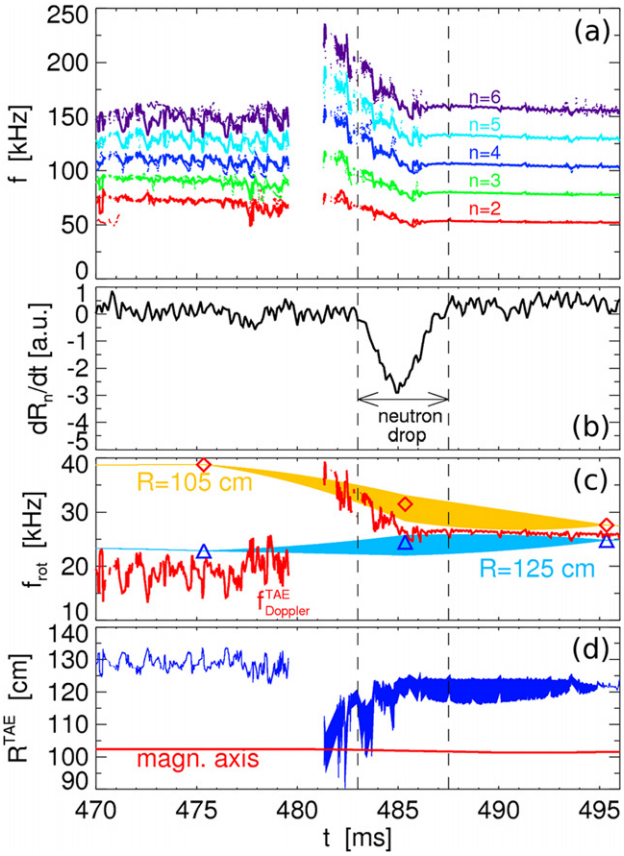

Figure 19. (*a*) Measured (dots) and reconstructed (solid line) frequencies for $n = 2, \ldots, 6$ TAEs. Reconstruction is obtained from $f_0^{\rm TAE}$ and $f^{\rm TAE}_{\rm Doppler}$ resulting from a linear fit of the measured $f^{\rm TAE}_{{\rm lab},n} = f^{\rm TAE}_{{\rm lab},n}(n)$. (*b*) Time derivative of the neutron rate. The negative dip, delimited by vertical dashed lines, indicates when fast ions are expelled from the plasma, possibly causing a transient drop in the toroidal rotation. (*c*) Measured rotation, with integration time of ~10 ms, at the plasma centre (diamonds) and at mid-radius (triangles). Shaded regions indicate different interpolations of the rotation evolution during the avalanche over short time scales. The maximum deviation around the measured values is ±10%. $f^{\rm TAE}_{\rm Doppler}$ is also shown for reference. (*d*) Sensitivity of the inferred $R^{\rm TAE}$ upon toroidal velocity evolution within the values in panel (*c*).

observed change in $f^{\rm TAE}_{{\rm lab},n}$ is caused by a decrease in $f_{\rm rot}$ (or, equivalently, in $f^{\rm TAE}_{\rm Doppler}$) only. The inferred $R^{\rm TAE}$ is also quite robust against uncertainties in the exact evolution of $f_{\rm rot}(R, t)$ (figures 19(*c*) and (*d*)), which is not directly measurable because of the long integration time (10 ms) of the CHERS system.

Based on the available data, the proposed interpretation for the evolution of $f_0^{\rm TAE}$ and $f^{\rm TAE}_{\rm Doppler}$ is that the dependence of $R^{\rm TAE}$ on the fast ion profile is partly lost during the avalanche. The cluster of TAEs locks instead on a perturbation which starts at the magnetic axis and then move outward (i.e. $R^{\rm TAE}$ shifts from the axis towards the edge, i.e. to regions with lower rotation) in the ~10 ms following the TAE burst. This scenario, suggestive of strong coupling between TAEs and low-frequency MHD, is indeed supported by the analysis of mode–mode coupling discussed in section 4. Further improvements (or corrections) to this interpretation would require data that are not presently available for NSTX plasmas. For instance, a fast CHERS system for measurements of $f_{\rm rot}$ on sub-millisecond time scales has recently been developed [35] and will be used to complement future investigations of the TAE dynamics during avalanches.

Along with the radial gradient, details of the fast ion distribution in velocity space, $F(E, p)$ (here E is the energy and p the pitch), also contribute to the TAE drive. However, a full experimental characterization of $F(E, p)$ is still missing and modelling is required. For MHD-quiescent plasmas, where fast ions are expected to behave classically, modelling can be accomplished with numerical tools such as the TRANSP/NUBEAM module [36]. An example is reported in figure 20, from which the complex nature of $F(E, p)$ for a realistic case with NB injection can be appreciated. Problems arise when fast ions and waves are expected to mutually influence each other and the modelling is required to be self-consistent, as in the case of strongly resonant TAEs. In this case, $F(E, p)$ will experience some distortion in either real or velocity space (or both). Neither the NUBEAM module mentioned above nor NOVA can model this interaction self-consistently. An anomalous fast ion diffusion coefficient can be introduced in TRANSP, but it rather represents a tool to mimic ad hoc losses in the simulation than a truly physics-driven model. For instance, rapid loss events may be collective rather than diffusive. Along with improvements in the fast ion

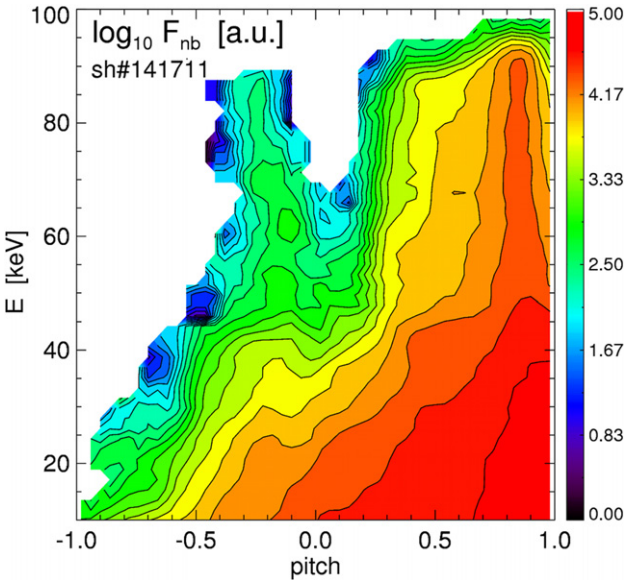

Figure 20. Fast ion distribution as a function of energy and pitch from TRANSP/NUBEAM [36] for discharge no. 141711, $t = 470$ ms and $R \approx 120$ cm.

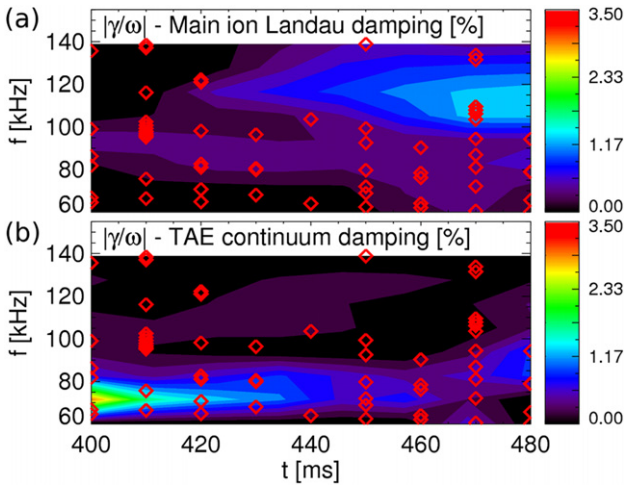

Figure 21. Dominant contributions to the linear damping rate from NOVA for a $n = 3$ TAE mode with $f \approx 100$ kHz. Symbols represent the actual eigenmodes found by NOVA. (*a*) Main ion Landau damping. (*b*) Continuum damping. Note the different trend with frequency of the different terms, which may result in local minima of the total damping.

diagnostics utilized in today's experiments, more sophisticated theories and codes are required. The comparison between experiments, quasi-linear modelling of the wave–particles interaction [37, 38] and/or non-linear and self-consistent codes (e.g. M3D-K [39, 40]) is beyond the scope of this paper, thus leaving the quantification of the $F(E, p)$ contribution to the TAE drive as an open issue.

The second, important element in determining the TAE stability is damping. Linear stability is calculated through NOVA (figure 21). Dominant terms in the total damping rate are continuum damping and ion Landau damping. Other terms, such as electron Landau damping, are negligible. Radiative damping is not considered here, because the model used in NOVA is inaccurate for high-β, low aspect ratio NSTX plasmas [41] and results may be unreliable.

An interesting result from figure 21 is that ion Landau damping and continuum damping are comparable in magnitude, but show different trends with frequency and time. Ion Landau damping is larger at higher frequency and increases in time because of the slight increase in ion temperature and density. In contrast, continuum damping is larger at lower frequency and decreases in time as the peak mode amplitude shifts to larger radii, away from the intersection with the continuum (figure 12). The opposite dependence of the two terms results in a minimum in frequency of the linear damping, which is in qualitative agreement with the observed mode frequency. Furthermore, the decreased damping at lower frequencies for increasing time may favour the down-chirp of the modes observed during the avalanche at $t \approx 480$ ms. More analysis is required to extend this analysis to the other modes observed in the experiment and verify the generality of these observations.

7. Summary and conclusions

This work has investigated two main aspects of chirping TAE modes on NSTX, namely (i) the mode's properties (namely frequency, amplitude, radial structure and the qualitative dependence on drive and damping terms) and (ii) the non-linear coupling between modes leading to the destabilization of low-frequency, kink-like activity.

Chirping parameters are rather constant among different scenarios, characterized by different schemes of additional heating (NB, rf) and confinement mode (L- versus H-mode). Bursting rates are $\approx$0.5–2 ms^{-1}. No systematic trend with thermal plasma and fast ion parameters is observed, except that larger bursts/chirps tend to be detected for increasing ratio of fast ion to thermal plasma pressure. The comparison with solutions from the NOVA code shows that, although the mode dynamics are complex, the mode structure is still reasonably well described by linear eigenmodes.

By studying the coupling between pairs of TAEs, one observes that the multi-mode TAE regime is prone to coupling with lower frequency modes, such as kinks or fishbones, which mediates the three-wave coupling between primary TAEs [12, 42]. The destabilization of otherwise stable kinks causes fast ion and thermal plasma losses that add to those caused by TAEs alone. The coupling between TAEs is favoured by their clustering around a similar radius. This is plausibly caused by the steep fast ion density gradient sustained at that location by NB injection. Similar conditions could be expected in fusion devices such as ITER. As a result of such non-linear TAE dynamics, an enhancement of fast ion loss or redistribution (in both velocity and real space) is expected. The radial mode extension can be used for a rough guess of whether fast ions are actually expelled or not from the core plasma. Significant losses are likely for global, radially extended TAEs with low n's, whereas more localized TAEs with high n's are more likely to cause redistribution. The latter case is predicted for the high toroidal field, large major radius plasmas of ITER [43]. However, even if no direct loss of fast ions is expected, redistribution itself can be a deleterious process in a reactor. First, modifications of the fast ion distribution may result in

unwanted variations of the non-inductive current profile [44]. Second, a relaxed fast ion pressure can impact the stability of other modes (e.g. kinks [45], sawteeth [46] and resistive wall modes [47]), thus affecting the overall plasma stability. Moreover, radial redistribution can enhance ripple-induced fast ion loss.

Future work will extend the comparison of measured mode properties and dynamics to predictions from the non-linear, self-consistent (M3D-K [39, 40]) code. For instance, preliminary simulations for NSTX-like plasmas were able to reproduce profile relaxation and significant multi-mode interactions, including the destabilization of otherwise stable, low-n modes [48].

Acknowledgments

Work supported by US DOE contract number DE-AC02-09CH11466.

References

[1] Cheng C.Z. *et al* 1986 Low-n Alfvén spectra in axisymmetric toroidal plasmas *Phys. Fluids* **29** 3695
[2] Fasoli A. *et al* 2007 Progress in the ITER physics basis: Chapter 5: Physics of energetic ions *Nucl. Fusion* **47** S264
[3] Zonca F. *et al* 2008 Nonlinear dynamics and complex behaviors in magnetized plasmas of fusion interest *Frontiers in Modern Plasma Physics* ed P.K. Shukla, B. Eliasson and L. Stenflo vol 34 (New York: American Institute of Physics) CP1061
[4] Fasoli A. *et al* 1998 Nonlinear splitting of fast particle driven waves in a plasma: observation and theory *Phys. Rev. Lett.* **81** 5564
[5] Heidbrink W.W. 1995 Beam-driven chirping instability in DIII-D *Plasma Phys. Control. Fusion* **37** 937
[6] Gryaznevich M.P. *et al* 2004 Beta-dependence of energetic particle-driven instabilities in spherical tokamaks *Plasma Phys. Control. Fusion* **46** S15
[7] Chirikov B.V. 1979 A universal instability of many-dimensional oscillator systems *Phys. Rep.* **52** 263
[8] Berk H.L. *et al* 1995 Numerical simulation of bump-on-tail instability with source and sink *Phys. Plasmas* **2** 3007
[9] Ono M. *et al* 2000 Exploration of spherical torus physics in the NSTX device *Nucl. Fusion* **40** 557
[10] Podestà M. *et al* 2009 Experimental studies on fast-ion transport by Alfvén wave avalanches on the National Spherical Torus Experiment *Phys. Plasmas* **16** 056104
[11] Fredrickson E.D. *et al* 2009 Modeling fast-ion transport during toroidal Alfvén eigenmode avalanches in the national spherical torus experiment *Phys. Plasmas* **16** 122505
[12] Podestà M. *et al* 2011 Non-linear dynamics of toroidicity-induced Alfvén eigenmodes on the National Spherical Torus Experiment *Nucl. Fusion* **51** 063035
[13] Cheng C.Z. 1992 Kinetic extensions of magnetohydrodynamics for axisymmetric toroidal plasmas *Phys. Rep.* **211** 1
[14] Medley S.S. *et al* 2004 MHD-induced energetic ion loss during H-mode discharges in the National Spherical Torus Experiment *Nucl. Fusion* **44** 1158
[15] Menard J.E. 2008 private communication, Princeton Plasma Physics Laboratory, Princeton, NJ
[16] Levinton F.M. *et al* 2008 The motional Stark effect diagnostic on NSTX *Rev. Sci. Instrum.* **79** 10F522
[17] Leblanc B.P. 2008 Thomson scattering density calibration by Rayleigh and rotational Raman scattering on NSTX *Rev. Sci. Instrum.* **79** 10E737
[18] Bell R.E. *et al* 2010 Comparison of poloidal velocity measurements to neoclassical theory on NSTX *Phys. Plasmas* **17** 082507
[19] Kim Y.C. *et al* 1979 Digital bispectral analysis and its applications to nonlinear wave interactions *IEEE Trans. Plasma Sci.* **7** 120
[20] Crocker N.A. *et al* 2011 High spatial sampling global mode structure measurements via multichannel reflectometry in NSTX *Plasma Phys. Control. Fusion* **53** 105001
[21] Lilley M.K. *et al* 2010 Effect of dynamical friction on nonlinear energetic particle modes *Phys. Plasmas* **17** 092305
[22] Lesur M. *et al* 2010 Spectroscopic determination of kinetic parameters for frequency sweeping Alfvén eigenmodes *Phys. Plasmas* **17** 122311
[23] Rosenbluth M.N. *et al* 1992 Mode structure and continuum damping of high-n toroidal Alfvén eigenmodes *Phys. Fluids* B **4** 2189
[24] Wang G. *et al* 2012 Simulation and adiabatic models for spontaneous frequency sweeping of energetic particle-driven Alfvén eigenmodes *Nucl. Fusion* submitted
[25] Fredrickson E.D. *et al* 2007 β suppression of Alfvén cascade modes in the National Spherical Torus Experiment *Phys. Plasmas* **14** 102510
[26] Zonca F. *et al* 2005 Transition from weak to strong energetic ion transport in burning plasmas *Nucl. Fusion* **45** 477
[27] Podestà M. *et al* 2010 Effects of toroidal rotation shear on toroidicity-induced Alfvén eigenmodes in NSTX *Phys. Plasmas* **17** 122501
[28] Strait E.J. *et al* 1994 Doppler shift of the TAE mode frequency in DIII-D *Plasma Phys. Control. Fusion* **36** 1211
[29] Bortolon A. *et al* 2011 Fast ion losses and redistribution induced by low frequency MHD in NSTX plasmas, based on FIDA observations and full-orbit simulations *2nd IAEA Technical Meeting on Energetic Particles in Magnetic Confinement Systems (Austin, TX)* http://w3fusion.ph.utexas.edu/ifs/iaeaep/talks/s5-012-bortolon-alessandro-ep-talk.pdf
[30] Yakovenko Y.V. *et al* 2010 Mode coupling of Alfvén instabilities *Nucl. Fusion* **50** 084015
[31] Podestà M. *et al* 2008 The NSTX fast-ion D-alpha diagnostic *Rev. Sci. Instrum.* **79** 10E521
[32] Heidbrink W.W. 2010 Fast-ion D-alpha measurements of the fast-ion distribution *Rev. Sci. Instrum.* **81** 10D727
[33] Heidbrink W.W. *et al* 2011 Characterization of off-axis fishbones *Plasma Phys. Control. Fusion* **53** 085028
[34] Marchenko V.S. *et al* 2011 Frequency chirping during a fishbone burst *Nucl. Fusion* **51** 122001
[35] Podestà M. *et al* 2012 A real-time velocity diagnostic for NSTX *Rev. Sci. Instrum.* **83** 033503
[36] Pankin A. *et al* 2004 The tokamak Monte Carlo fast ion module NUBEAM in the National Transport Code Collaboration library *Comput. Phys. Commun.* **159** 157
[37] Berk H.L. *et al* 1995 Line broadened quasi-linear burst model *Nucl. Fusion* **35** 1661
[38] Ghantous K. *et al* 2011 Quasilinear model for energetic particle interaction with TAE modes *12th IAEA Technical Meeting on Energetic Particles in Magnetic Confinement Systems (Austin, TX)* http://w3fusion.ph.utexas.edu/ifs/iaeaep/
[39] Park W. *et al* 1999 Plasma simulation studies using multilevel physics models *Phys. Plasmas* **6** 1796
[40] Lang J. *et al* 2009 Gyrokinetic ∂f particle simulations of toroidicity-induced Alfvén eigenmode *Phys. Plasmas* **16** 102101
[41] Berk H.L. *et al* 1993 Arbitrary mode number boundary-layer theory for nonideal toroidal Alfvén modes *Phys. Fluids* B **5** 3969
[42] Crocker N.A. *et al* 2006 Three-wave interactions between fast-ion modes in the National Spherical Torus Experiment *Phys. Rev. Lett.* **97** 045002

[43] Gorelenkov N.N. *et al* 2005 Beam anisotropy effect on Alfvén eigenmode stability in ITER-like plasmas *Nucl. Fusion* **45** 226
[44] Gerhardt S.P. *et al* 2011 Calculation of the non-inductive current profile in high-performance NSTX plasmas *Nucl. Fusion* **51** 033004
[45] Porcelli F. *et al* 1994 Solution of the drift-kinetic equation for global plasma modes and finite particle orbit widths *Phys. Plasmas* **1** 470
[46] Graves J.P. *et al* 2010 Experimental verification of sawtooth control by energetic particles in ion cyclotron resonance heated JET tokamak plasmas *Nucl. Fusion* **50** 052002
[47] Berkery J.W. *et al* 2010 The role of kinetic effects, including plasma rotation and energetic particles, in resistive wall mode stability *Phys. Plasmas* **17** 082504
[48] Fu G.-Y. 2007 Nonlinear hybrid simulations of multiple energetic particle driven Alfvén modes in toroidal plasmas *49th Annual Meeting of the Division of Plasma Physics (Orlando FL 2007)* paper BI2, http://meetings.aps.org/Meeting/DPP07/